Supplementary Information (SI) for Journal of Materials Chemistry C.

Supplementary Information for

Congested position isomerism enhanced mechanoluminescence of triarylboranes

Yangbin Xie,[a, ‡] Yujie Zhou,[b, ‡] Yan-Ting Zhang,[a] Hanting Zhou,[a] Zhenghua Ju,[a] Shenlong Jiang,[c] Chun-Lin Sun,[a, *] Jincai Wu,[a] Qun Zhang,[b, c, *] and Xiaobo Pan[a, *]

[a] Y. Xie, Y. Zhang, H. Zhou, Z. Ju, Prof. C. Sun, Prof. J. Wu, Prof. X. Pan.
State Key Laboratory of Applied Organic Chemistry (Lanzhou University), Key Laboratory of Nonferrous Metal Chemistry and Resources Utilization of Gansu Province, College of Chemistry and Chemical Engineering, Lanzhou University, Lanzhou 730000, People's Republic of China.
[b] Y. Zhou, Prof. Q. Zhang.
Hefei National Research Center for Physical Sciences at the Microscale, Department of Chemical Physics, University of Science and Technology of China, Hefei, Anhui 230026, P. R. China.
[c] S. Jiang, Prof. Q. Zhang.
Hefei National Laboratory, University of Science and Technology of China, Hefei, Anhui 230088, P. R. China.
* Corresponding Authors: boxb@lzu.edu.cn; suncl@lzu.edu.cn; qunzh@ustc.edu.cn

‡ These authors contributed equally to this work.

Table of Contents

Figure S28 Difference electrostatic potential (ESP) analysis of ***o*-NAB-*α***, ***o*-NAB-*β***, ***m*-NAB**, and ***p*-NAB** in gas state.

References

Experimental Section

Reagents and materials

Unless otherwise noted, all the chemicals were purchased from commercial sources and used without further purification. Dry tetrahydrofuran was obtained through the distillation over sodium and benzophenone. Compounds **Mes_2BF**,[1] **R1**,[2] **R2**,[3] ***o*-NAB**[4], and **R4**[5] were synthesized according to previously reported procedures.

The preparation of Crystals

According to our previous work,[4] sample ***o*-NAB** could be slowly evaporated and crystallized in dichloromethane (CH_2Cl_2) at room temperature to obtain orange ***o*-NAB-*α*** crystals, and in mixture solution of CH_2Cl_2 and n-hexane at -25 ºC to give colorless ***o*-NAB-*β*** crystals. Colorless ***m*-NAB** crystals can be obtained by evaporating crystallization in ethyl acetate (EA) at room temperature. Colorless ***p*-NAB** crystals can be obtained by evaporating crystallization in CH_2Cl_2/n-hexane at 0 ºC.

Instrumentation and measurements

^{1}H NMR, ^{13}C NMR and ^{11}B NMR were recorded in $CDCl_3$ on a JEOL JNM-ECS-400 MHz spectrometer, tetramethylsilane was used as the internal standard. The solid-state ^{13}C and ^{11}B CP-MAS NMR spectra were recorded on an Agilent 600 DD2 spectrometer (Agilent, USA, magnetic field strength 14.1 T). The powder samples were placed in a pencil-type zirconia rotor of 4.0 mm o.d. FT-IR spectra were carried out using a Bruker Vertex 70 by using conventional KBr pellets method. The attenuation total reflection infrared spectroscopy (ATR-FTIR) were recorded on a Thermo Fisher Scientific Nicolet iS20. Crystal structures were solved by direct methods using Olex 2-1.2. Subsequent difference Fourier analyses and least-squares refinement with SHELXL-2014/7 program package allowed for the location of the atom position.[6-8] Powder X-Ray diffraction patterns were performed on an Rigaku D/Max-2400 X-ray diffractometer (XRD) with Cu Kα radiation (λ = 1.54184 Å) at 25 °C (scan range: 5−50°). Single crystal data was collected on a Rigaku Oxford Diffraction using mirror monochromated Mo Kα radiation (λ = 0.71073 Å). UV-vis absorption spectra were recorded on a Lambda 950 recording spectrophotometer. The SEM images were recorded on a CIQTEK SEM3200. The photoluminescence (PL) spectra were measured on a Horiba FluoroMax-4 spectrofluorometer (Horiba Scientific). The lifetimes were recorded with an Edinburgh FLS 920 combined fluorescence lifetime and steady state spectrometer equipped with a hydrogen lamp and a microsecond flash-lamp (μF920H), respectively. Mean decay times (τ_{avg}) were obtained from individual lifetimes τ_i and amplitudes B_i of multi-exponential evaluation. The total lifetimes of multi-sectioned PL-decay spectra are calculated using the following equation:

$$\tau_{\mathrm{avg}} = \frac{\sum_{i=1}^{n} B_i \tau_i^2}{\sum_{i=1}^{n} B_i \tau_i}$$

$$\varphi_2 = \frac{B_2\tau_2}{B_1\tau_1 + B_2\tau_2 + B_3\tau_3} \cdot 100\%$$

where τ is the lifetime, i represents for the number of the lifetime components, and B_i is the proportion for each lifetime components, φ is percentage of the relative fluorescence intensity.

The femtosecond time-resolved transient absorption (TA) measurements were performed under ambient conditions on a Helios pump-probe system (Ultrafast Systems LLC) in combination with an amplified femtosecond laser system (Coherent). The 400 nm pump pulses (~50 nJ/pulse at the sample, corresponding to a pump fluence of ~70 μJ/cm^2 given the typical focus radii of ~150 μm) were delivered by an optical parametric amplifier (TOPAS-800-fs), which was excited by a Ti:sapphire regenerative amplifier (Legend Elite-1K-HE; center wavelength 800 nm, pulse duration 35 fs, pulse energy 3 mJ, repetition rate 1 kHz) seeded with a mode−locked Ti:sapphire laser system (Micra 5) and pumped with a 1-kHz Nd:YLF laser (Evolution 30). The white-light continuum (WLC) probe pulses were generated by focusing the 800-nm beam (split from the regenerative amplifier) onto a sapphire plate. A reference beam split from the WLC was used to correct the pulse-to-pulse fluctuation. The time delays (within 8 ns) between the pump and probe pulses were varied by a motorized optical delay line. The instrument response function (IRF) was determined to be ~100 fs. A mechanical chopper operating at 500 Hz was used to modulate the TA spectra with and without the pump pulses can be recorded alternately. The samples sandwiched between two 1 mm thick quartz plates were placed on the sample table.

Complementary video

Take a few of ***o*-NAB** crystals and place them on a glass slide. Under 365 nm UV lamp irradiation, they exhibited cold white light. When gently ground with a spoon, the powder exhibits bright blue light. After fuming the glass slide in CH_2Cl_2 vapor, the PL intensity will significantly decrease. The "grinding − CH_2Cl_2 fuming" process was repeated twice recorded in this video.

Computational detail

Time-dependent density-functional theory (TD-DFT) calculations were performed on Gaussian 09 program (Revision D09).[9] The ground state (S_0) geometries were optimized with the Becke's three-parameter exchange functional along with the Lee Yang Parr's correlation functional (B3LYP) using 6-31G(d) basis sets. The optimization for crystalphase geometry in the ground state (S_0) was first performed on the central molecule while the adjacent molecules were fixed in the initial geometries using the DFT method. Based on the optimized S_0 geometry, the vertical excitation energies and the optimized geometry in the first excited state (S_1) were also calculated using the TD-DFT method.

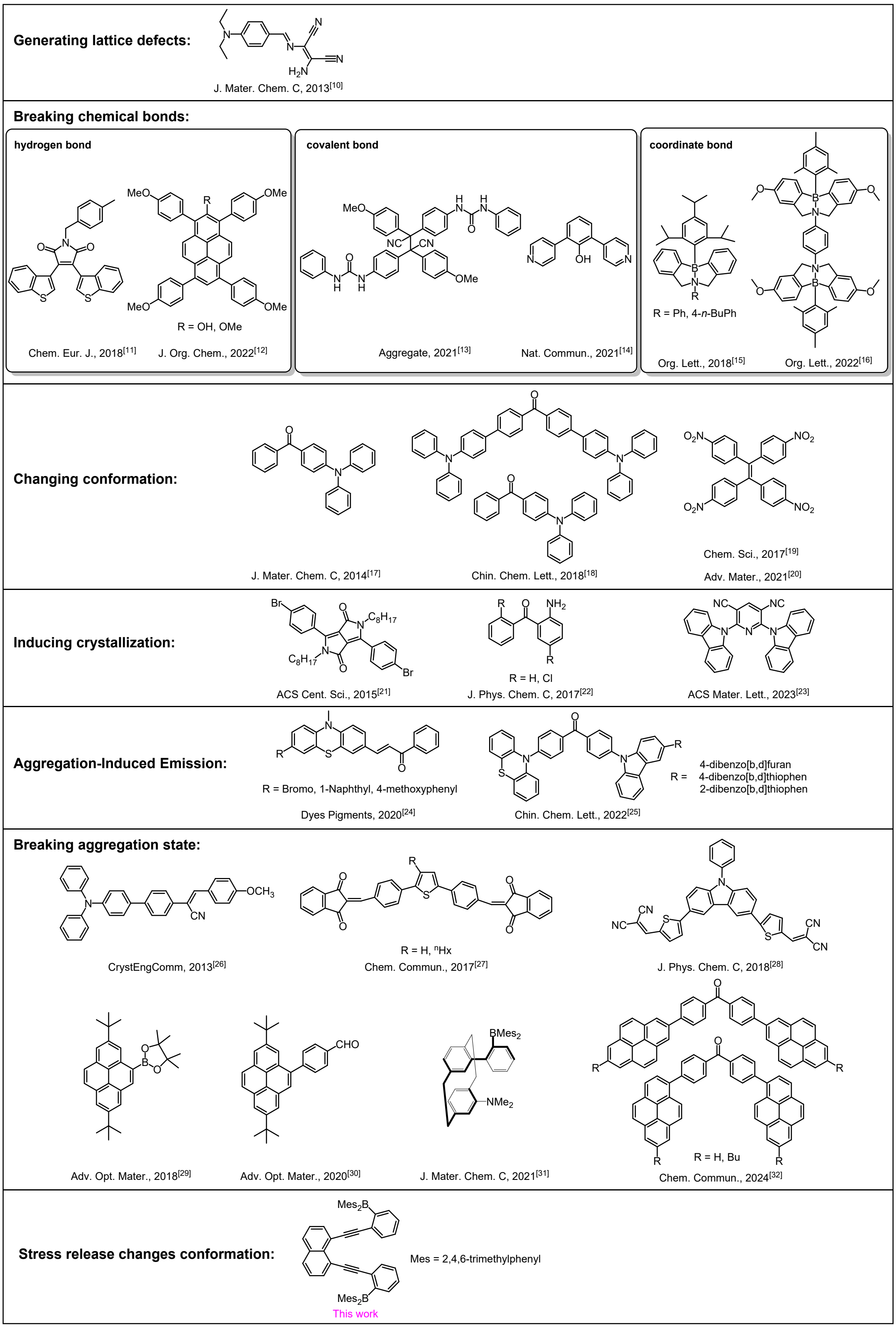

Scheme S1. Summary of previously reported organic molecules with mechanoluminescence enhancement (MLE) properties.

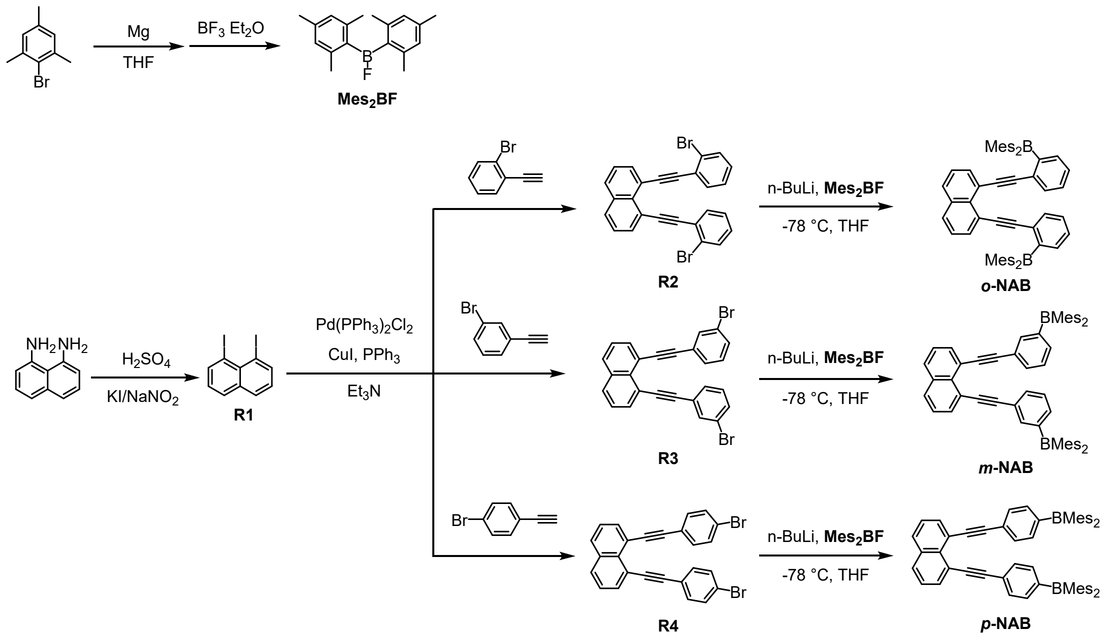

Scheme S2. Synthetic routes of triarylboron derivatives.

Synthesis of 1,8-bis[(3-bromophenyl)ethynyl]naphthalene (R3): According to previously reported procedures, a mixture of **R1** (2.0 g, 5.26 mmol), 3-bromophenylethyne (2.86 g, 15.8 mmol), $PdCl_2(PPh_3)_2$ (0.10 g), CuI (0.10 g), PPh_3 (0.10 g) and Et_3N (40 mL) in a Shrek bottle at ambient temperature was purged with nitrogen for 5 minutes. The sealed bottle was heated at 50 °C for 24 hours. After filtration and removal of the solvent, the residue was subjected to chromatography on silica gel. Elution with petroleum ether/ethyl acetate (20/1, Rf: 0.6) gave light yellow powder. Yield: 2.35 g (92%). ^1H NMR (400 MHz, $CDCl_3$, 293 K): δ 7.91 − 7.79 (m, 4H), 7.47 (t, J = 7.7 Hz, 4H), 7.34 (d, J = 8.1 Hz, 2H), 7.29 (d, J = 7.7 Hz, 2H), 7.03 (t, J = 7.9 Hz, 2H). ^{13}C NMR (101 MHz, $CDCl_3$, 293 K): δ 135.09, 134.12, 131.34, 130.12, 129.50, 125.73, 125.63, 122.08, 120.31, 95.08, 90.95.

Synthesis of 1,8-bis{[3-(dimesitylboranyl)phenyl]ethynyl}naphthalene (*m*-NAB): Under anaerobic and anhydrous conditions, n-BuLi (7.6 mL, 12.2 mmol, 1.6 M in hexanes) was added dropwise to a stirred THF solution of **R3** (2.90 g, 6.0 mmol) at −78 °C for 4 hours, and then **Mes_2BF** (3.22 g, 12.0 mmol) in THF (15 mL) was slowly added. Subsequently, the reaction mixture was slowly warmed to room temperature and stirred overnight. After the addition of water, the solution was then extracted with dichloromethane. The crude product was then purified by column chromatography (CH_2Cl_2/petroleum ether: 1/5, Rf: 0.8) to afford ***m*-NAB**. Yield: 3.17 g (64%). ^1H NMR (400 MHz, $CDCl_3$, 293 K): δ 7.82 (d, J = 7.1 Hz, 2H), 7.79 (d, J = 8.2 Hz, 2H), 7.70 (s, 2H), 7.42 (t, J = 7.7 Hz, 2H), 7.32 (d, J = 7.3 Hz, 4H), 6.93 (t, J = 7.6 Hz, 2H), 6.81 (s, 8H), 2.30 (s, 12H), 1.98 (s, 24H). ^{13}C NMR (101 MHz, $CDCl_3$, 293 K): δ 141.56, 140.88, 138.92, 138.66, 135.72, 135.18, 134.99, 134.17, 131.52, 129.62, 128.35, 127.77, 125.60, 123.72, 120.86, 96.96, 89.87, 23.55, 21.30. ^{11}B NMR (128.3 MHz, $CDCl_3$, 293 K): δ 71.09.

Synthesis of 1,8-bis{[4-(dimesitylboranyl)phenyl]ethynyl}naphthalene (*p*-NAB): Under anaerobic and anhydrous conditions, n-BuLi (7.6 mL, 12.2 mmol, 1.6 M in hexanes) was added dropwise to a stirred THF solution of **R4** (2.90 g, 6.0 mmol) at −78 °C for 4 hours, and then **Mes_2BF** (3.22 g, 12.0 mmol) in THF (15 mL) was slowly added. Subsequently, the reaction mixture was slowly warmed to room temperature and stirred overnight. After the addition of water, the solution was then extracted with dichloromethane. The crude product was then purified by column chromatography (ethyl acetate/petroleum ether: 1/12, Rf: 0.7) to afford ***p*-NAB**. Yield: 3.27 g (66%). ^{1}H NMR (400 MHz, $CDCl_3$, 293 K): δ 7.89 (d, J = 7.2 Hz, 2H), 7.85 (d, J = 7.2 Hz, 2H), 7.51 − 7.44 (m, 2H), 7.39 (d, J = 8.2 Hz, 4H), 7.32 (d, J = 8.2 Hz, 4H), 6.78 (s, 8H), 2.30 (s, 12H), 1.91 (s, 24H). ^{13}C NMR (101 MHz, $CDCl_3$, 293 K): δ 141.60, 140.88, 138.81, 136.05, 135.86, 135.49, 134.14, 132.93, 131.22, 131.14, 131.07, 129.92, 128.32, 128.24, 127.18, 125.81, 125.69, 120.76, 97.46, 92.12, 23.50, 21.35. ^{11}B NMR (128.3 MHz, $CDCl_3$, 293 K): δ 75.82.

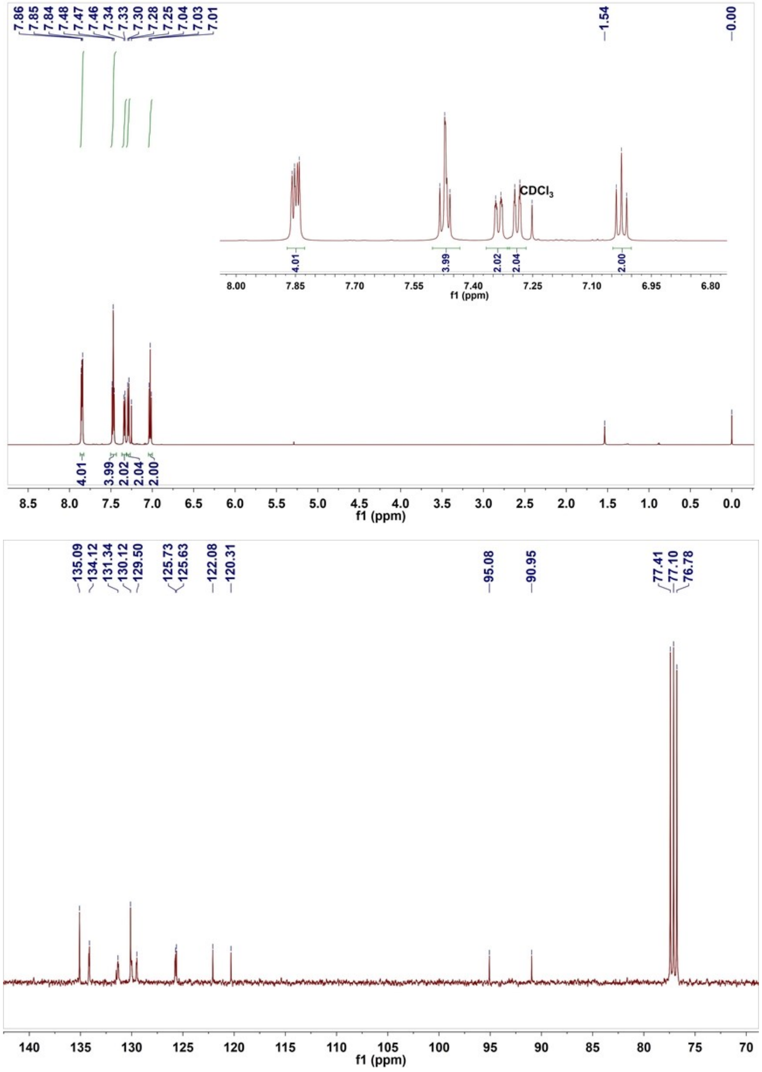

Figure S1. The ^{1}H (top, 400 MHz) and ^{13}C (bottom, 101 MHz) NMR spectra of **R3** were recorded in $CDCl_3$ at room temperature.

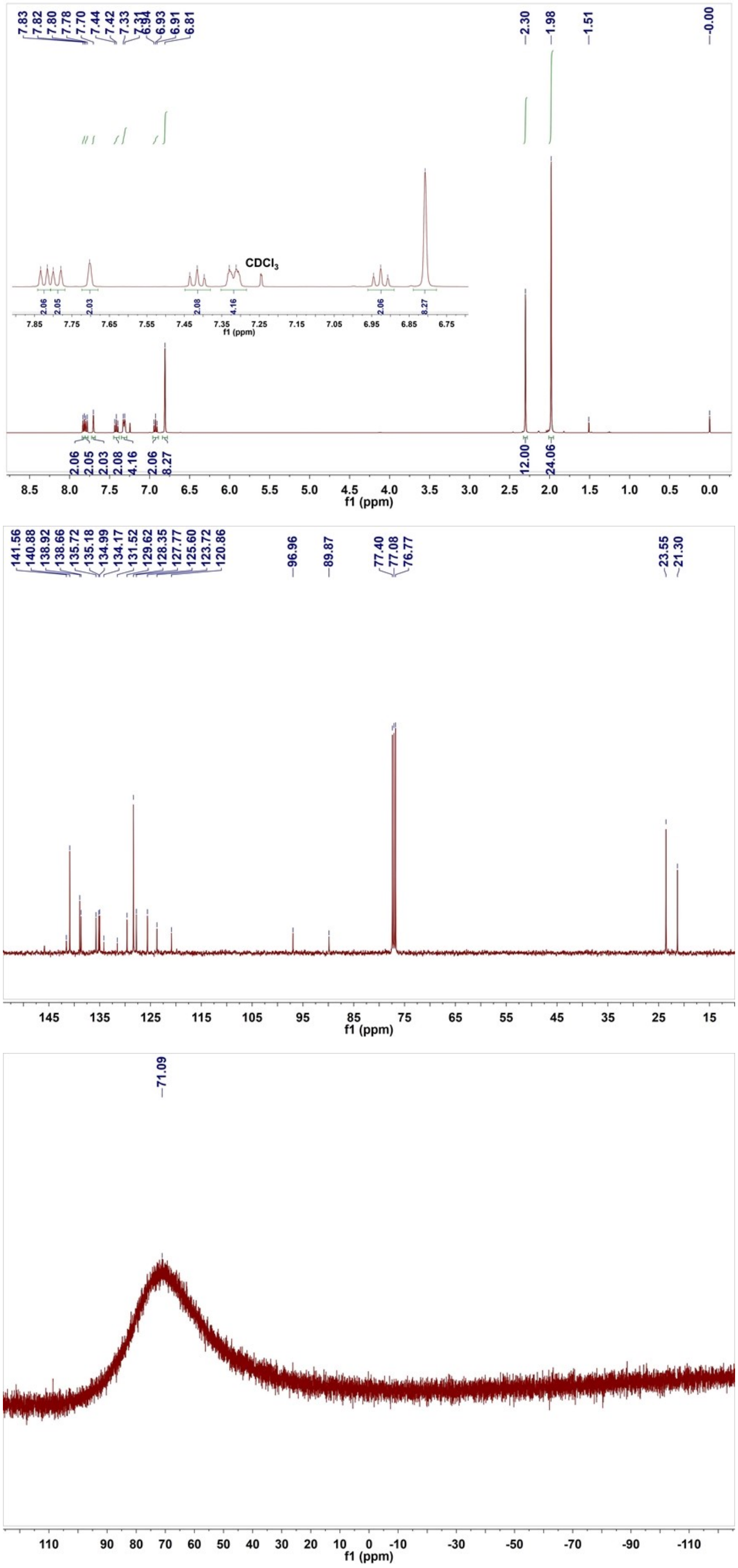

Figure S2. The ^{1}H (top, 400 MHz), ^{13}C (middle, 101 MHz) and ^{11}B (bottom, 128.3 MHz) NMR spectra of ***m*-NAB** were recorded in CDCl$_3$ at room temperature.

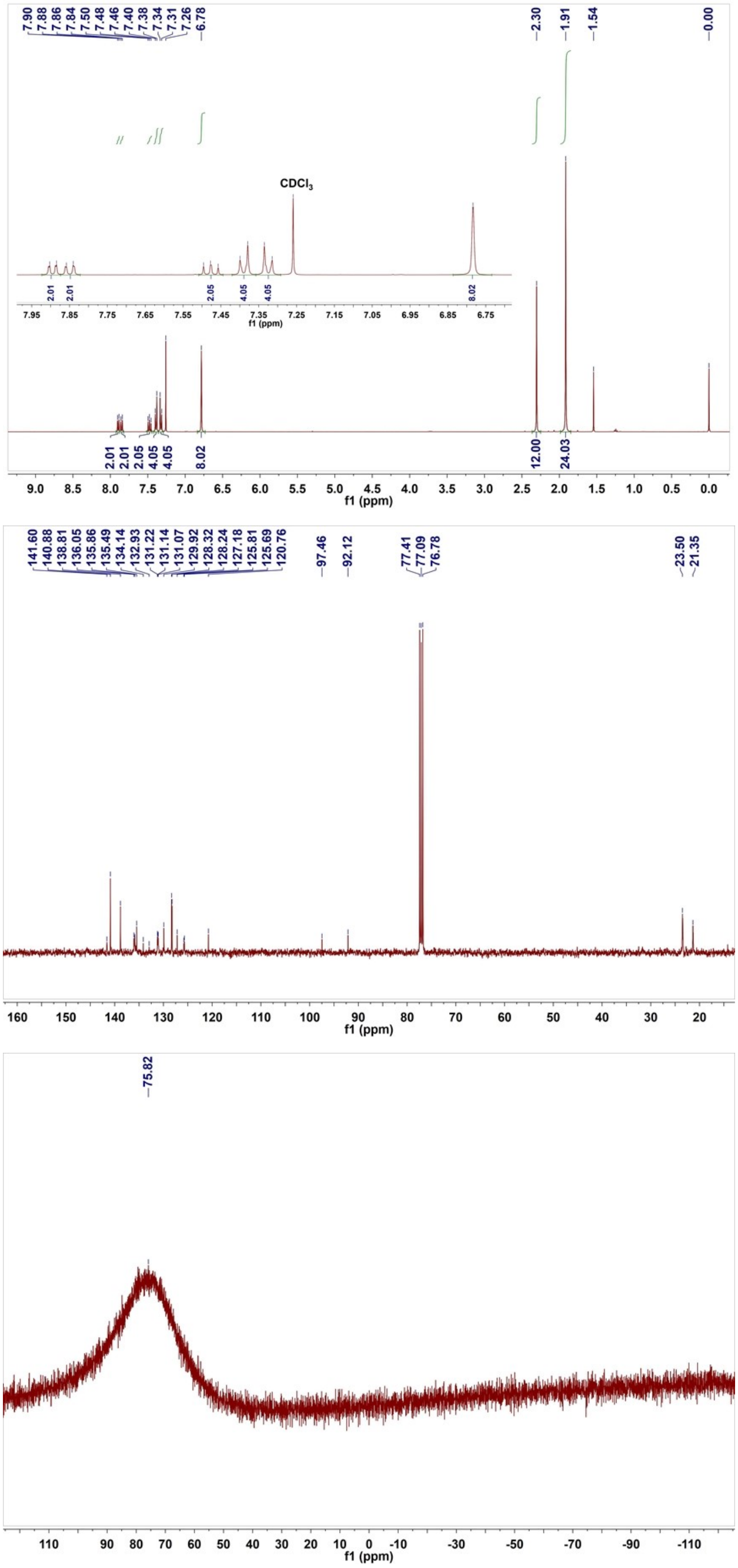

Figure S3. The ^{1}H (top, 400 MHz), ^{13}C (middle, 101 MHz) and ^{11}B (bottom, 128.3 MHz) NMR spectra of ***p*-NAB** were recorded in $CDCl_3$ at room temperature.

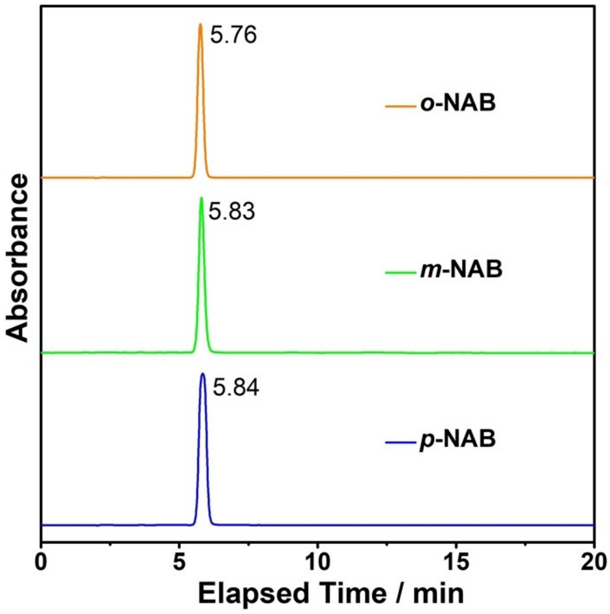

Figure S4. HPLC was recorded at the peak absorption of 390 nm for ***o*-NAB**, ***m*-NAB** and ***p*-NAB** (c), (Solvent and flow rate: H_2O/THF = 2/8, 1 mL/min).

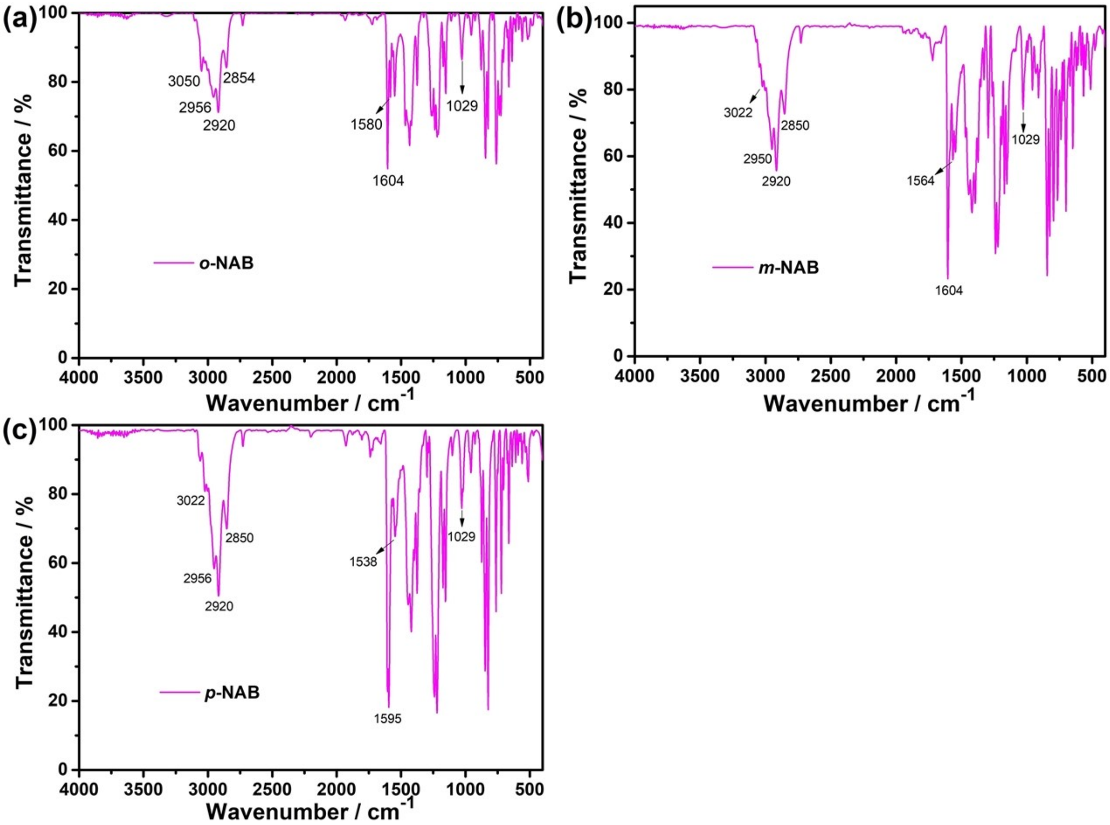

Figure S5. FT-IR spectra of ***o*-NAB** (a), ***m*-NAB** (b) and ***p*-NAB** (c) under ambient conditions.

Table S1. Single-crystal X-ray diffraction data of ***o*-NAB-*α***,[4] ***o*-NAB-*β***, ***m*-NAB**, and ***p*-NAB**.

Name	***o*-NAB-*α***	***o*-NAB-*β***	***m*-NAB**	***p*-NAB**
Formula	$C_{62}H_{58}B_2$	$C_{64}H_{62}B_2Cl_4$	$C_{62}H_{58}B_2$	$C_{62}H_{58}B_2$
Mr (g mol^{-1})	824.70	994.55	824.70	824.70
T / K	150(2)	149.99(11)	304.15(10)	304.13(10)
Crystal system	monoclinic	monoclinic	triclinic	orthorhombic
Space group	$P2_1/n$	$P2_1/n$	P-1	$Pca2_1$
a (Å)	14.1665(9)	8.46950(10)	13.82200(10)	12.3766(7)
b (Å)	14.8565(9)	22.7720(3)	14.6804(2)	15.5432(9)
c (Å)	22.7151(13)	31.9259(4)	14.9499(2)	29.1517(19)
α (°)	90	90	65.4920(10)	90
β (°)	99.9310(3)	95.8880(10)	71.5950(10)	90
γ (°)	90	90	66.7590(10)	90
V (Å^3)	4709.1(5)	6124.98(13)	2493.94(6)	5608.0(6)
Z	4	4	2	4
ρ_{calc} (g cm^{-3})	1.163	1.079	1.098	0.977
μ (mm^{-1})	0.484	2.014	0.457	0.054
F(000)	1760	2096	880	1760
R_{int}	0.0670	0.0718	0.0219	0.0825
GOF^c	1.036	1.345	1.086	0.978
R_1^a, wR_2^b ($I > 2\sigma(I)$)	0.0497, 0.0619	0.0962, 0.1041	0.0437, 0.1314	0.0961, 0.1493
R_1^a, wR_2^b (all date)	0.1216, 0.1315	0.3026, 0.3137	0.0500, 0.1373	0.2539, 0.2908
CCDC	1817523	2413338	2413344	2413345

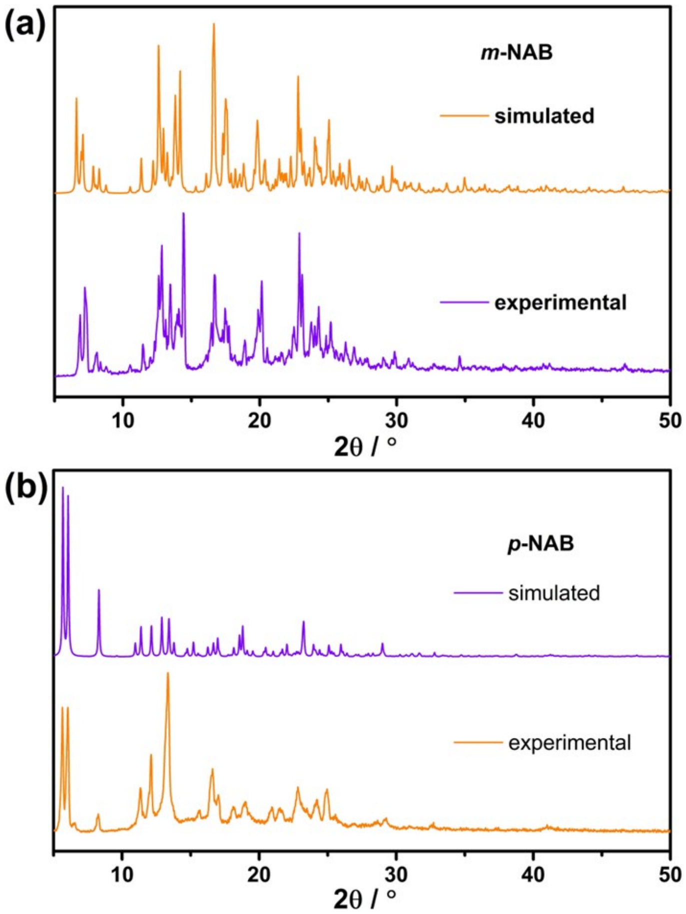

Figure S6. PXRD patterns of ***m*-NAB** and ***p*-NAB** (as-synthesis: organic, from single crystal data: violet).

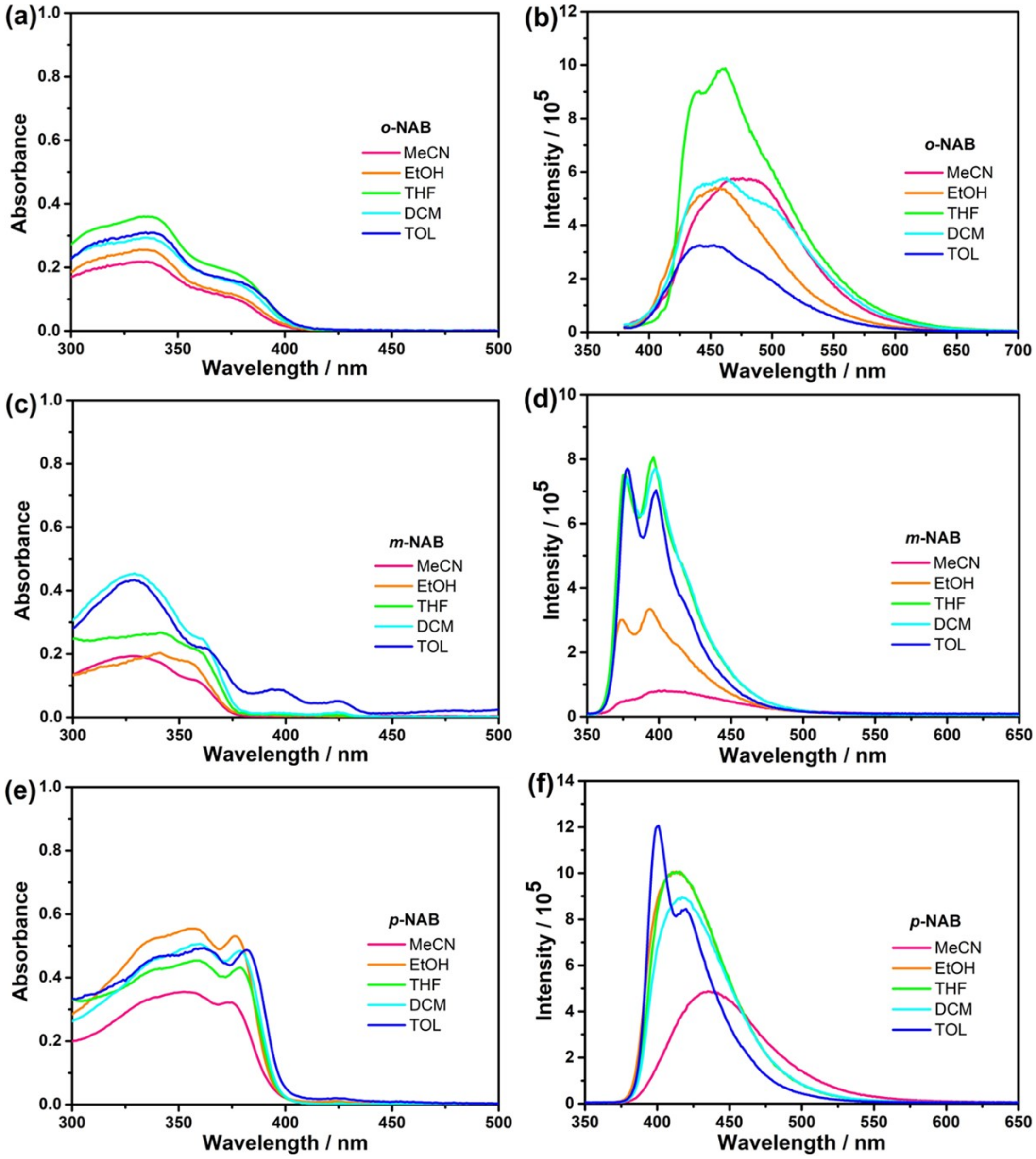

Figure S7. UV-vis absorption and PL spectra of ***o*-NAB** (a, b), ***m*-NAB** (c, d) and ***p*-NAB** (e, f) in different polarities solvents under ambient conditions (*C* = 10 μM, ***o*-NAB**: λ_{ex} = 365 nm, ***m*-NAB** and ***p*-NAB**: λ_{ex} = 330 nm).

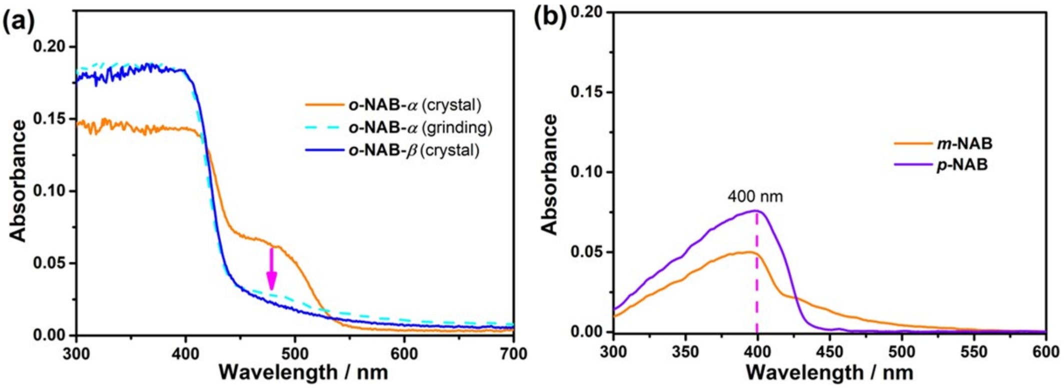

Figure S8. (a) The solid UV-vis absorption spectra of ***o*-NAB-*α*** crystals, grinding ***o*-NAB-*α*** powder and ***o*-NAB-*β*** crystals under ambient conditions. (b) The solid UV-vis absorption spectra of ***m*-NAB** and ***p*-NAB** crystals under ambient conditions.

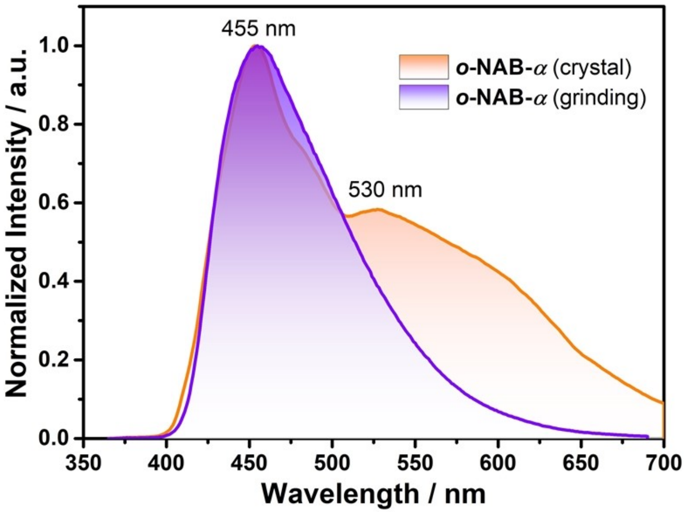

Figure S9. Normalized emission spectra of ***o*-NAB-*α*** crystals and grinding powder at 365 nm excitation wavelength.

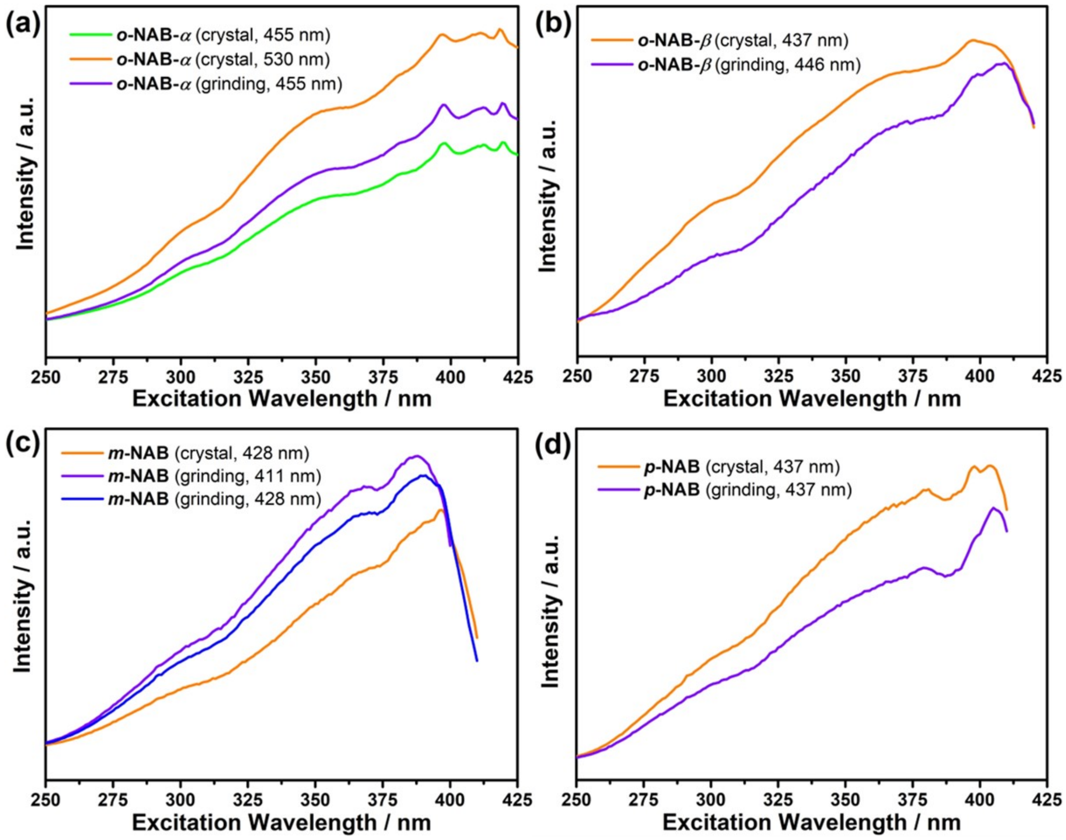

Figure S10. The corresponding excitation spectra of ***o*-NAB-*α*** (a), ***o*-NAB-*β*** (b), ***m*-NAB** (c) and ***p*-NAB** (d) in crystal and grinding powder state.

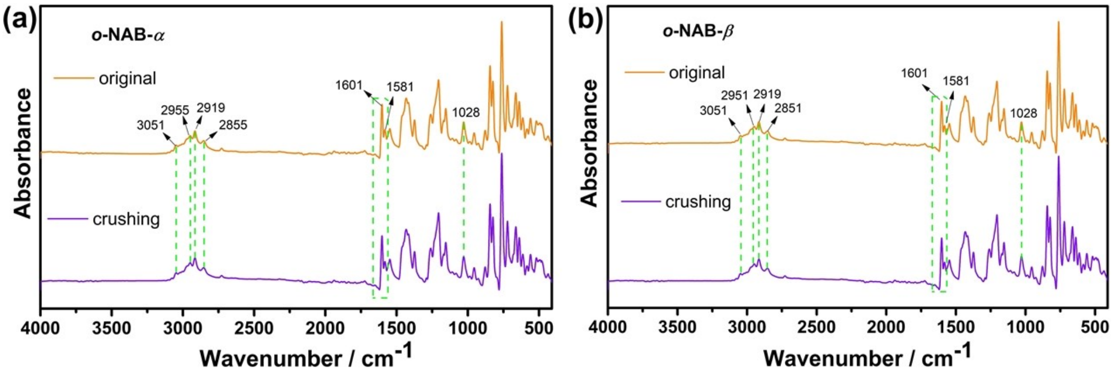

Figure S11. ATR-FTIR spectra of ***o*-NAB-*α*** (a) and ***o*-NAB-*β*** (b) before and after crushing.

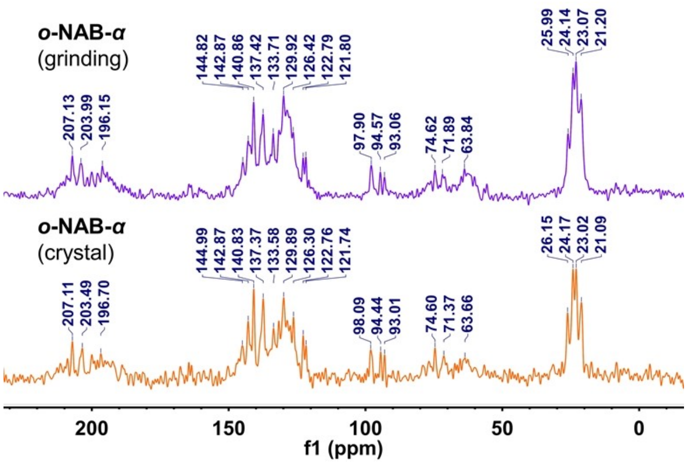

Figure S12. Solid ^{13}C CP-MAS NMR spectra of ***o*-NAB-*α*** crystals (orange) and grinding ***o*-NAB-*α*** powder (purple).

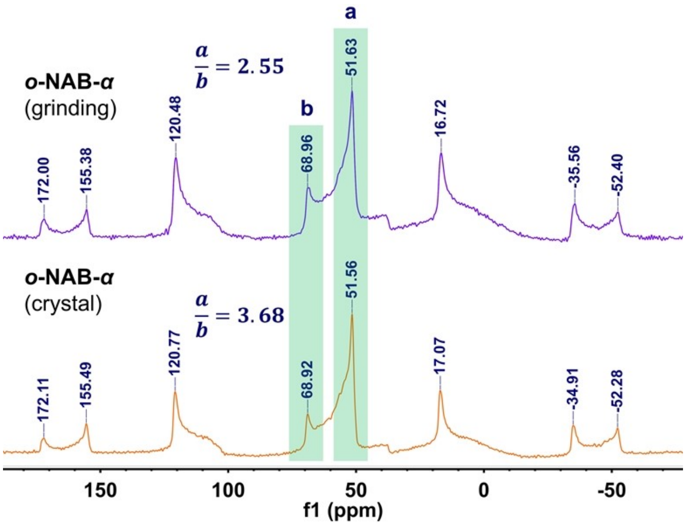

Figure S13. Solid ^{11}B CP-MAS NMR spectra of ***o*-NAB-*α*** crystals (orange) and grinding ***o*-NAB-*α*** powder (purple).

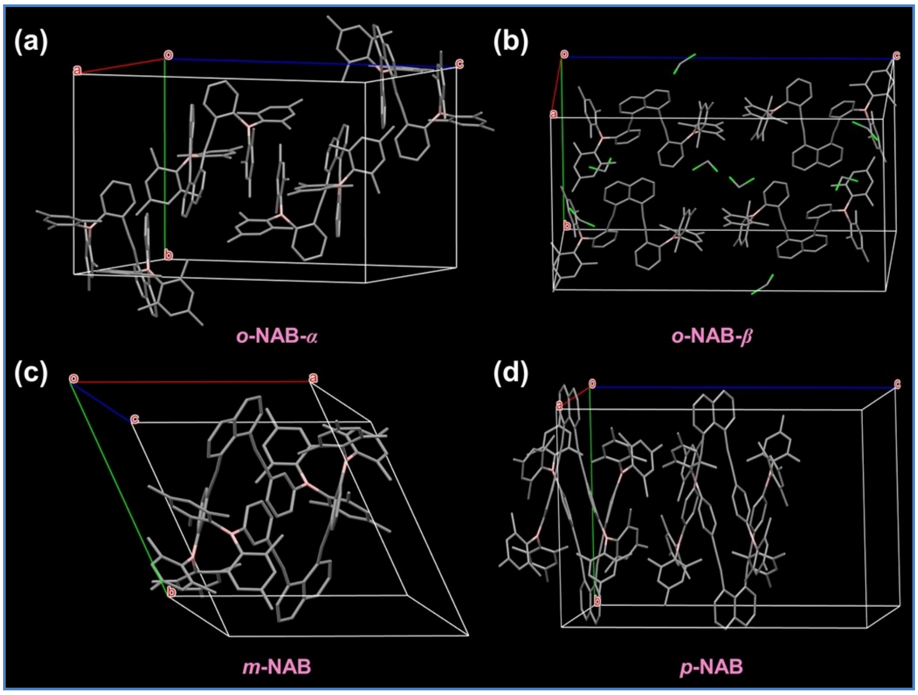

Figure S14. Crystal cell stacking diagrams of ***o*-NAB-*α*** (a), ***o*-NAB-*β*** (b), ***m*-NAB** (c) and ***p*-NAB** (d), all H atoms in the structures were omitted for clarity (Solvent CH_2Cl_2 exists in ***o*-NAB-*β*** crystals).

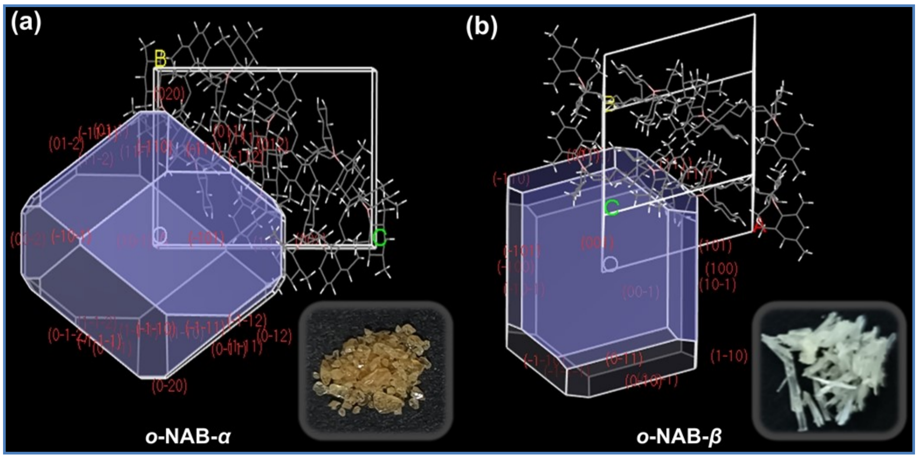

Figure S15. Sketch maps of crystals graph and predicted morphology for ***o*-NAB-*α*** (a) and ***o*-NAB-*β*** (b) based on the actual crystal structures. The important Miller index facets are labeled with their Miller indices.

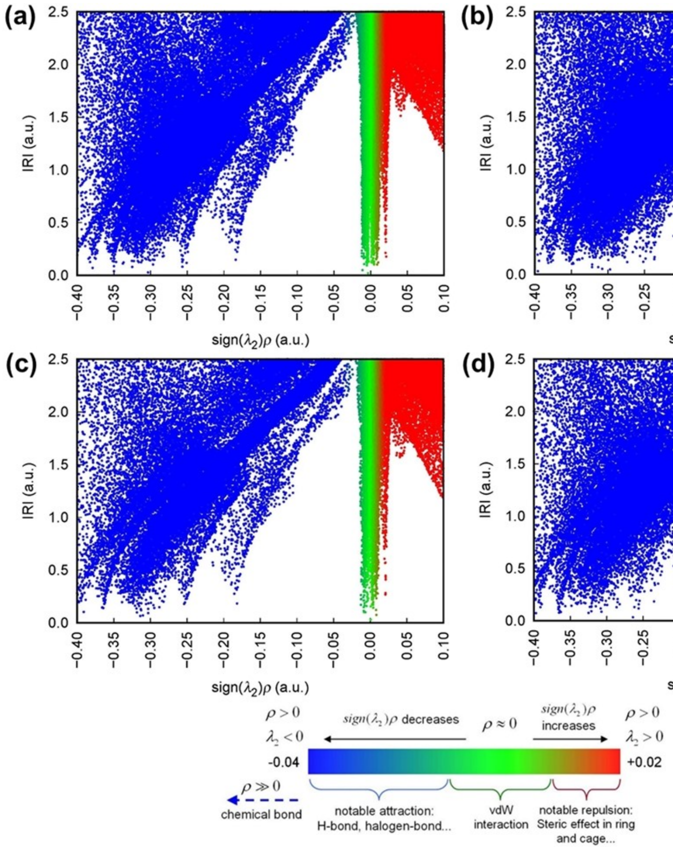

Figure S16. Scatter plot of isosurface distribution about ***o*-NAB-*α***, ***o*-NAB-*β***, ***m*-NAB** and ***p*-NAB**.

Table S2. PL lifetimes (τ) of ***o*-NAB-*α***, ***o*-NAB-*β***, ***m*-NAB** and ***p*-NAB** at corresponding emission wavelengths under the crystal and grinding powder state, respectively.

Entry	State	λ_{em} (nm)	B_1	τ_1 (ns)	B_2	τ_2 (ns)	τ_{avg} (ns)	χ^2
o*-NAB-*α	crystal	455	0.043	0.298	5×10^{-4}	3.185	0.6	1.131
o*-NAB-*α	crystal	530	0.043	0.279	0.001	3.997	1.2	1.171
o*-NAB-*α	powder	455	0.021	0.572	0.004	2.313	1.3	1.038
o*-NAB-*β	powder	437	0.027	0.354	0.004	2.054	1.1	1.111
o*-NAB-*β	crystal	446	0.014	1.434	0.003	2.558	1.7	1.022
***m*-NAB**	crystal	428	0.013	1.988	-	-	2.0	1.139
***m*-NAB**	powder	411	0.010	0.259	0.012	1.688	1.5	1.087
***m*-NAB**	powder	428	0.014	1.779	1×10^{-4}	5.433	1.9	1.163
***p*-NAB**	crystal	437	0.019	1.174	0.001	2.953	1.4	1.047
***p*-NAB**	powder	437	0.020	0.857	0.001	2.518	1.1	1.088

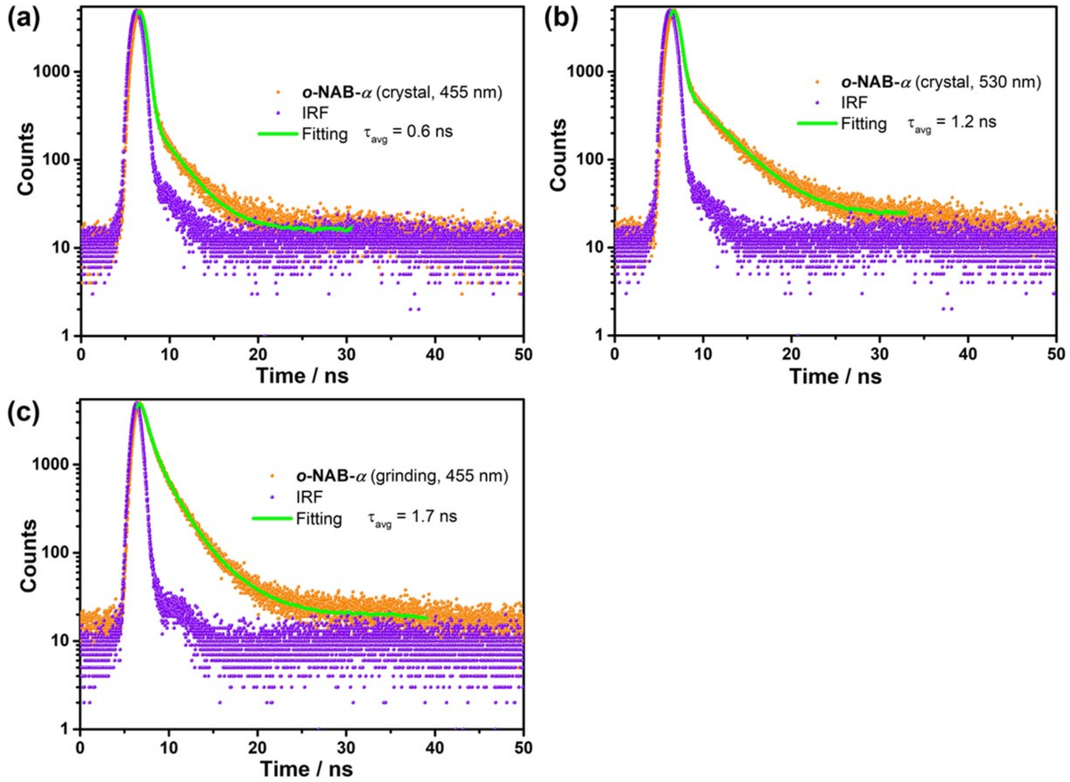

Figure S17. Transient PL decay curves of ***o*-NAB-*α*** crystals (λ_{em} = 455 nm, 530 nm) and grinding powder (λ_{em} = 455 nm) at 365 nm excitation wavelength.

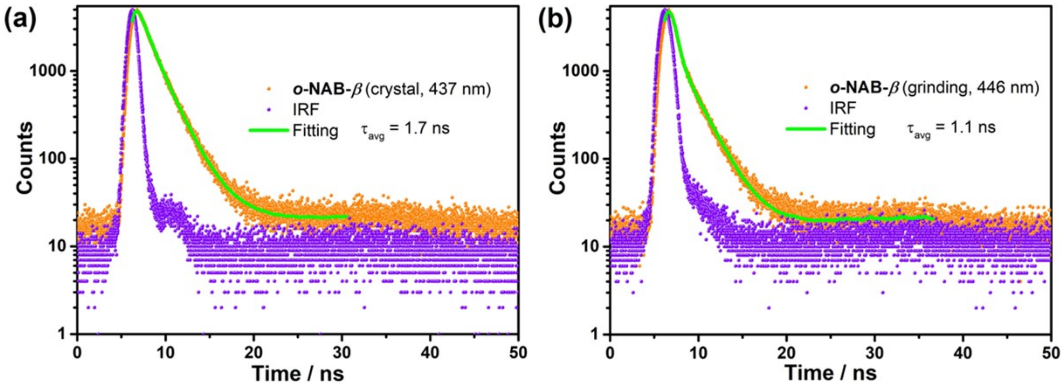

Figure S18. Transient PL decay curves of ***o*-NAB-*β*** crystals (λ_{em} = 437 nm) and grinding powder (λ_{em} = 446 nm) at 365 nm excitation wavelength.

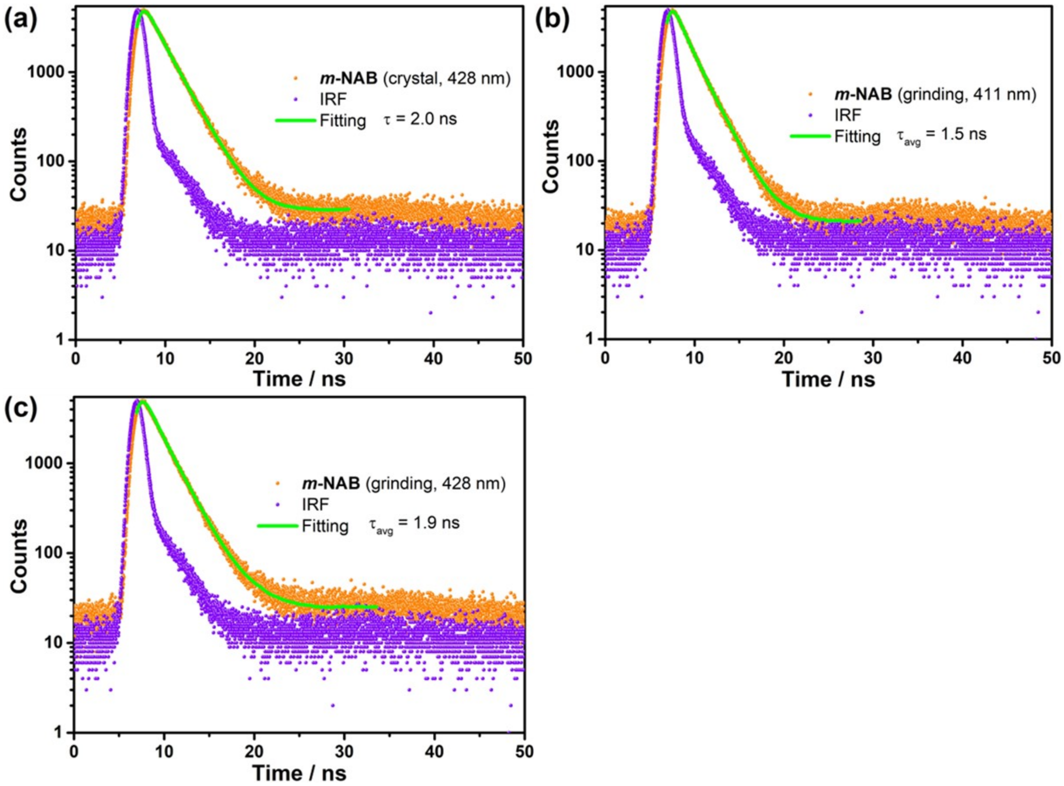

Figure S19. Transient PL decay curves of ***m*-NAB** crystals (λ_{em} = 428 nm) and grinding powder (λ_{em} = 411 nm, 428 nm) at 365 nm excitation wavelength.

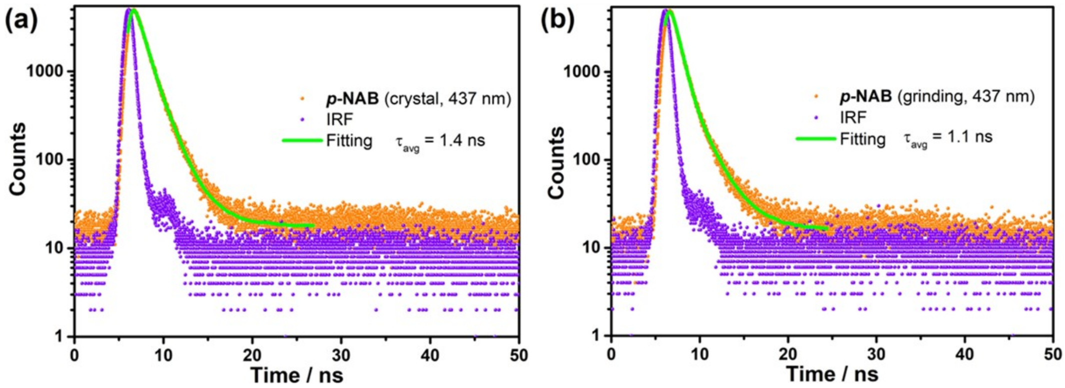

Figure S20. Transient PL decay curves of ***p*-NAB** crystals and grinding powder at 365 nm excitation wavelength (λ_{em} = 437 nm).

Table S3. Photophysical parameters of ***o*-NAB-*α***, ***o*-NAB-*β***, ***m*-NAB** and ***p*-NAB** crystals.

Entry	State	λ_{em} (nm)	τ_{ave} (ns)	Φ (%)	k_r (s^{-1})	k_{nr} (s^{-1})
o*-NAB-*α	crystal	455	0.6	0.7	1.2×10^7	1.7×10^7
	powder	455	1.7	12.6	7.4×10^7	5.1×10^6
o*-NAB-*β	crystal	437	1.7	23.5	1.4×10^8	4.5×10^6
	powder	446	1.1	15.3	1.4×10^8	7.7×10^6
***m*-NAB**	crystal	428	1.1	64.5	5.9×10^8	3.2×10^6
	powder	428	1.9	63.3	3.3×10^8	1.9×10^6
***p*-NAB**	crystal	437	1.4	38.3	2.7×10^8	4.4×10^6
	powder	437	1.1	27.8	2.5×10^8	6.6×10^6

Note: $k_r = \Phi / \tau$; $k_{nr} = (1-\Phi) / \tau$.

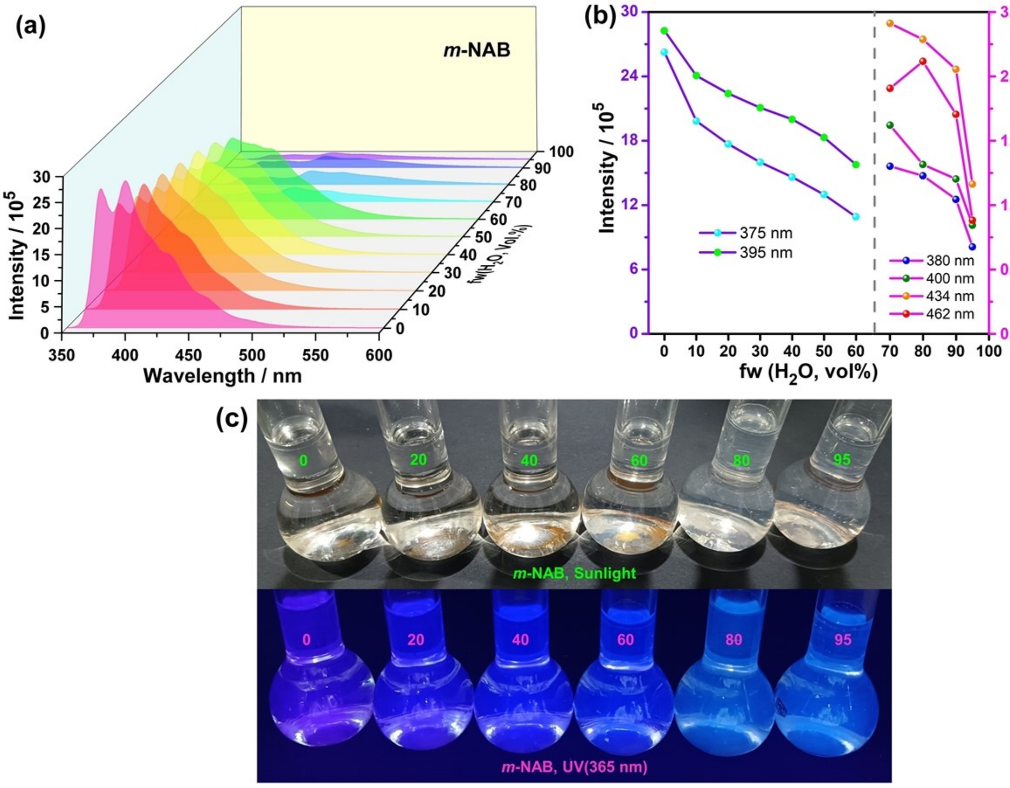

Figure S21. (a) PL spectra of ***m*-NAB** in THF/H_2O mixtures with different f_w at 330 nm excitation wavelength. (b) Plot of PL intensity and emission wavelength of ***m*-NAB** in THF/H_2O mixtures with different f_w at 330 nm excitation wavelength. (c) Photos of ***m*-NAB** in THF/H_2O mixtures taken under the irradiation of a 365 nm UV lamp. (f_w = 0 − 95%, C = 10 μM).

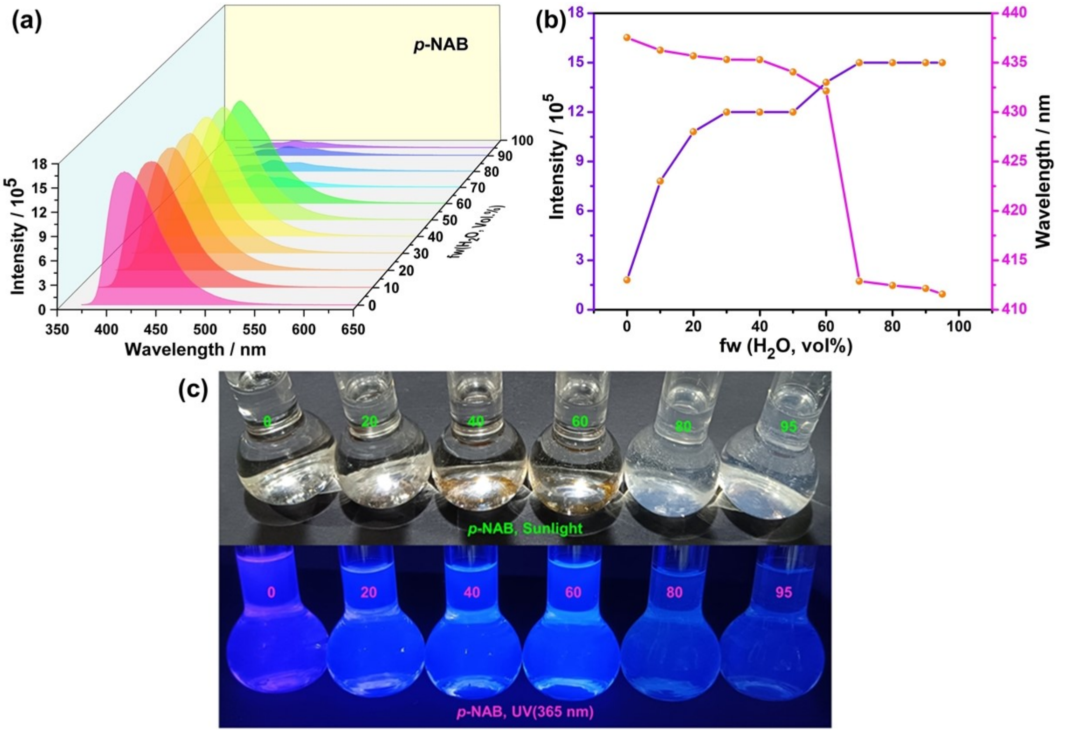

Figure S22. (a) PL spectra of ***p*-NAB** in THF/H_2O mixtures with different f_w at 350 nm excitation wavelength. (b) Plot of PL intensity and emission wavelength of ***p*-NAB** in THF/H_2O mixtures with different f_w at 350 nm excitation wavelength. (c) Photos of ***p*-NAB** in THF/H_2O mixtures taken under the irradiation of a 365 nm UV lamp. (f_w = 0 − 95%, C = 10 μM).

Table S4. The emission wavelength, PL lifetime and quantum yields about compounds ***o*-NAB**, ***m*-NAB** and ***p*-NAB** in THF/water mixtures with different water volume fractions at 365 nm excitation wavelength (f_w = 0% and 95%, C = 10 μM).

Compound	f_w (H_2O, Vol.%)	λ_{em} (nm)	τ_i (ns)	B_i	Rel. (%)	χ^2	τ_{avg} (ns)	Φ (%)
***o*-NAB**	0	464	0.7392 10.1388	0.043 0.001	84.64 15.36	1.135	3.0	4.8
	95	458	0.7555 3.4681 9.7005	0.019 0.011 0.002	20.97 54.70 24.33	0.995	4.6	18.2
***m*-NAB**	0	375	3.3453	0.023	100.00	1.165	/	40.8
		395	3.3230	0.023	100.00	1.130	/	
	95	380	0.2201 1.8960	0.058 0.0003	95.25 4.75	1.182	0.3	14.0
		400	0.2766 2.1288	0.045 0.001	89.68 10.32	1.184	0.5	
		434	0.8076 3.6498 10.4892	0.015 0.014 0.001	16.68 71.97 11.36	1.048	4.1	
		462	1.1717 3.8373 10.6540	0.011 0.014 0.001	16.00 70.49 13.52	1.051	4.3	
***p*-NAB**	0	413	1.5857	0.029	100.00	1.177	/	68.3
	95	435	0.4618 3.1130 7.2848	0.039 0.009 0.001	32.82 49.72 17.46	1.145	2.8	21.9

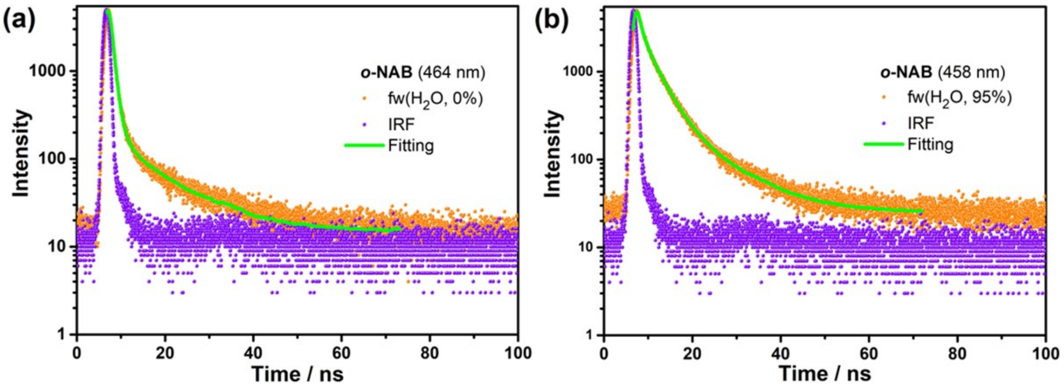

Figure S23. Transient PL decay curves of ***o*-NAB** in THF/water mixtures with different water volume fractions (f_w = 0 and 95%) at room temperature.

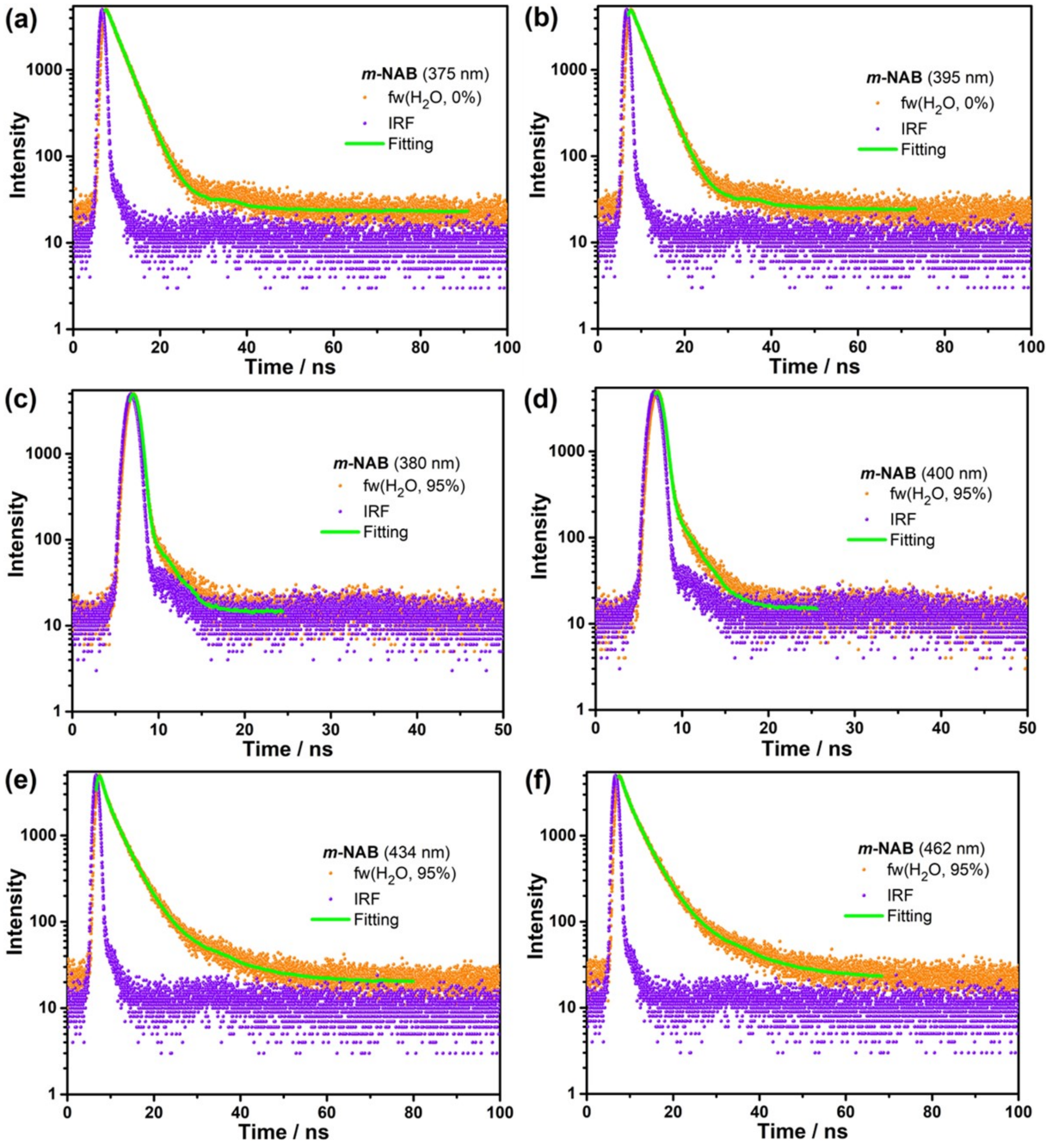

Figure S24. Transient PL decay curves of ***m*-NAB** in THF/water mixtures with different water volume fractions (f_w = 0 and 95%) at room temperature.

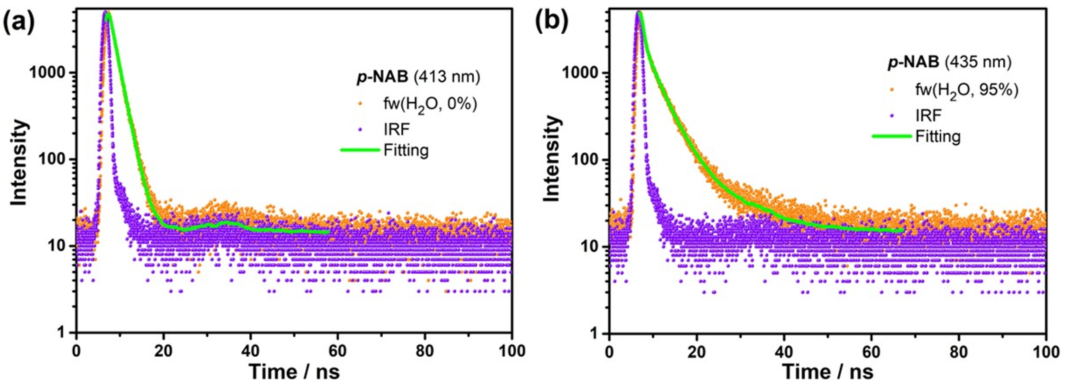

Figure S25. Transient PL decay curves of ***p*****-NAB** in THF/water mixtures with different water volume fractions (f_w = 0 and 95%) at room temperature.

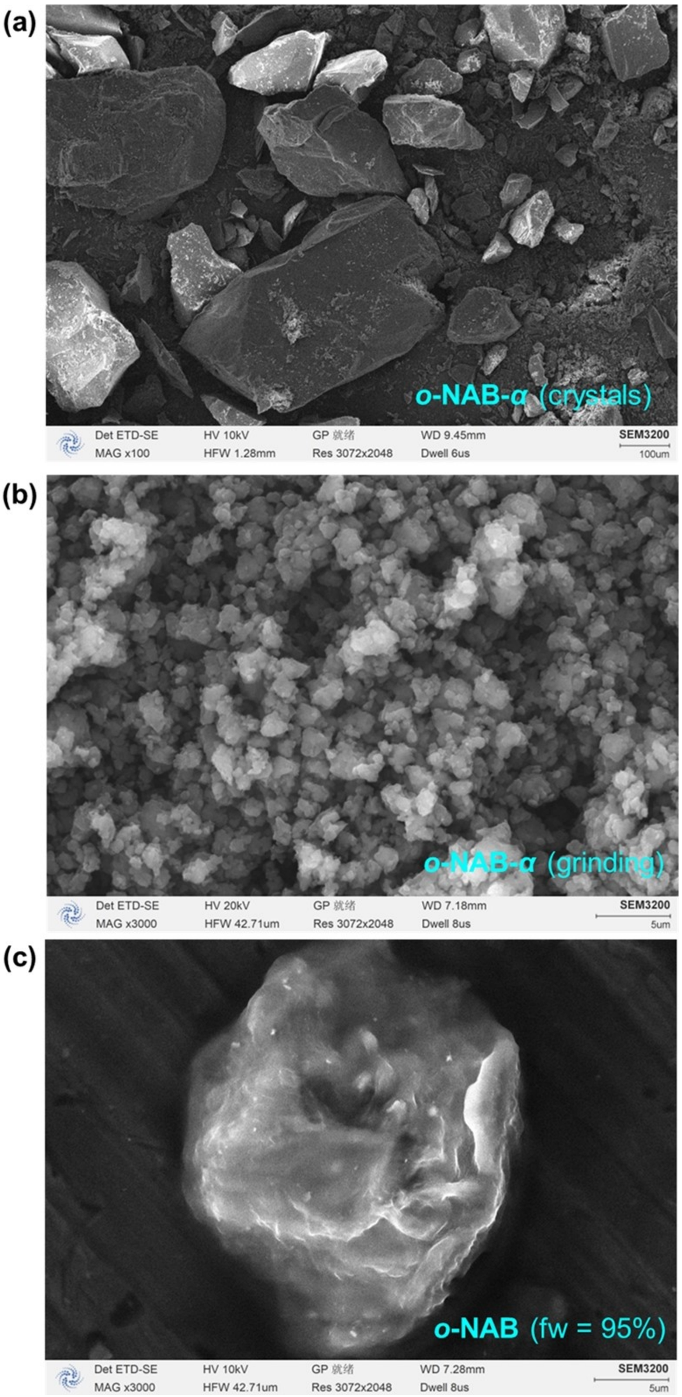

Figure S26. SEM images for ***o*-NAB-*α*** crystals (a), grinding ***o*-NAB-*α*** powder (b) and ***o*-NAB** in THF/water mixtures solution with water volume fraction of 95% (c), respectively.

Table S5. Global fitting results of TA kinetics in the probing wavelength range of 580−640 nm using 7 traces with a 10-nm interval for ***o*-NAB-*α*** crystals, grinding ***o*-NAB-*α*** powder, grinding ***o*-NAB-*β*** powder, and ***o*-NAB-*β*** crystals.

Entry	State	τ_1 (ps)	τ_2 (ps)	τ_3 (ps)	τ_{avg} (ps)
o*-NAB-*α	crystal	0.40 (32.3%)	38.4 (27.3%)	336 (40.4%)	314
o*-NAB-*α	powder	1.90 (53.8%)	21.9 (39.5%)	510 (6.7%)	402
o*-NAB-*β	powder	3.39 (41.0%)	48.2 (37.1%)	476 (21.9%)	409
o*-NAB-*β	crystal	3.81 (30.4%)	48.7 (39.3%)	532 (30.3%)	478

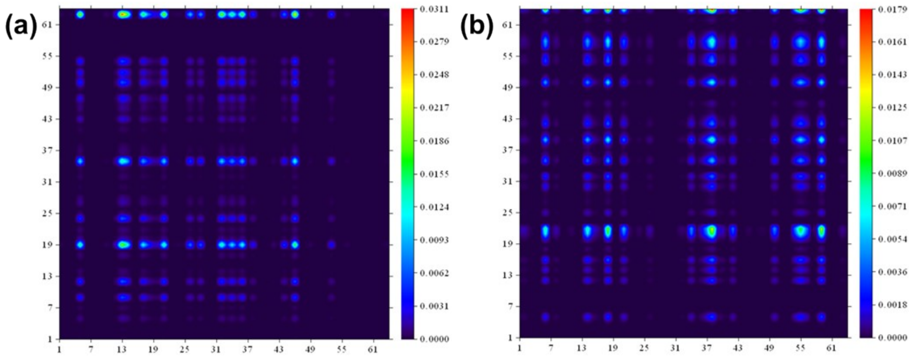

***m*-NAB** ***p*-NAB**

Figure S27. The transition density matrix of the S_1 state for ***m*-NAB** and ***o*-NAB** calculated at B3LYP/6-31G(d).

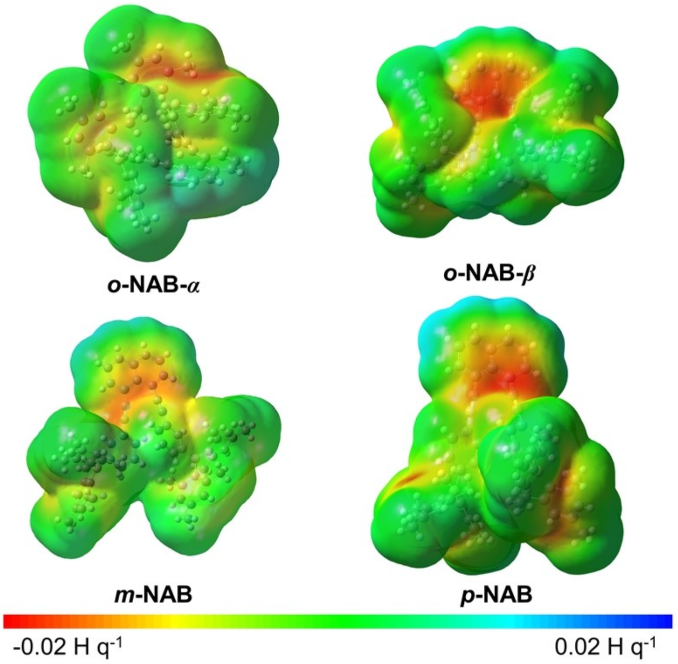

Figure S28. Difference electrostatic potential (ESP) analysis of ***o*-NAB-*α***, ***o*-NAB-*β***, ***m*-NAB** and ***p*-NAB** in gas state. The potential energy range is -0.02 to 0.02 H q^{-1} for all surfaces shown, red indicates areas with dense electron density, yellow for normal, while blue areas suggest less electron density.

References

[1] E. L. Coz, Z. Zhang, T. Roisnel, L. Cavallo, L. Falivene, J.-F. Carpentier, Y. Sarazin, *Chem. Eur. J.* **2020**, *26*, 3535−3544.

[2] D. Ahmadli, Y. Sahin, E. Calikyilmaz, O. Şahin, Y. E. Türkmen, *J. Org. Chem.* **2022**, *87*, 6336−6346.

[3] Y.-T. Wu, T. Hayama, K. K. Baldridge, A. Linden, J. S. Siegel, *J. Am. Chem. Soc.* **2006**, *128*, 6870−6884.

[4] J. Zhao, C. Ru, Y. Bai, X. Wang, W. Chen, X. Wang, X. Pan, J. Wu, *Inorg. Chem.* **2018**, *57*, 12552−12561.

[5] X. Chen, J. Jin, Y. Wang, P. Lu, *Chem. Eur. J.* **2011**, *17*, 9920−9923.

[6] O. V. Dolomanov, L. J. Bourhis, R. J. Gildea, J. A. K. Howard, H. Puschmann, *J. Appl. Crystallogr.* **2009**, *42*, 339−341.

[7] G. M. Sheldrick, *Acta Crystallogr., Sect. A: Found. Crystallogr.* **2008**, *64*, 112−122.

[8] G. M. Sheldrick, *Acta Crystallogr., Sect. A: Found. Adv.* **2015**, *71*, 3−8.

[9] M. J. Frisch, G. W. Trucks, H. B. Schlegel, G. E. Scuseria, M. A. Robb, J. R. Cheeseman, G. Scalmani, V. Barone, B. Mennucci, G. A. Petersson, H. Nakatsuji, M.Caricato, X. Li, H. P. Hratchian, A. F. Izmaylov, J. Bloino, G. Zheng, J. L. Sonnenberg, M. Hada, M. Ehara, K. Toyota, R. Fukuda, J. Hasegawa, M. Ishida, T. Nakajima, Y. Honda, O. Kitao, H. Nakai, T. Vreven, J. A. Montgomery Jr., J. E. Peralta, F. Ogliaro, M. Bearpark, J. J. Heyd, E. Brothers, K. N. Kudin, V. N. Staroverov, T. Keith, R. Kobayashi, J. Normand, K. Raghavachari, A. Rendell, J. C. Burant, S. S. Iyengar, J. Tomasi, M. Cossi, N. Rega, J. M. Millam, M. Klene, J. E. Knox, J. B. Cross, V. Bakken, C. Adamo, J. Jaramillo, R. Gomperts, R. E. Stratmann, O. Yazyev, A. J. Austin, R. Cammi, C. Pomelli, J. W. Ochterski, R. L. Martin, K. Morokuma, V. G. Zakrzewski, G. A. Voth, P. Salvador, J. J. Dannenberg, S. Dapprich, A. D. Daniels, O. Farkas, J. B. Foresman, J. V. Ortiz, J. Cioslowski and D. J. Fox, Gaussian 09, D.01 Gaussian, Inc., Wallingford CT, **2013**.

[10] T. Han, Y. Hong, N. Xie, S. Chen, N. Zhao, E. Zhao, J. W. Y. Lam, H. H. Y. Sung, Y. Dong, B. Tong, B. Z. Tang, *J. Mater. Chem. C* **2013**, *1*, 7314−7320.

[11] J. Wang, Z. Liu, S. Yang, Y. Lin, Z. Lin, Q. Ling, *Chem. Eur. J.* **2018**, *24*, 322−326.

[12] X. Wang, J. Zhang, X. Mao, Y. Liu, R. Li, J. Bai, J. Zhang, C. Redshaw, X. Feng, B. Z. Tang, *J. Org. Chem.* **2022**, *87*, 8503−8514.

[13] J. Kida, D. Aoki, H. Otsuka, *Aggregate* **2021**, *2*, e50.

[14] Z. Li, Y. Wang, G. Baryshnikov, S. Shen, M. Zhang, Q. Zou, H. Ågren, L. Zhu, *Nat. Commun.* **2021**, *12*, 908−915.

[15] Q. Hou, L. Liu, S. K. Mellerup, N. Wang, T. Peng, P. Chen, S. Wang, *Org. Lett.* **2018**, *20*, 6467−6470.

[16] Y. Shi, C. Li, H. Ma, Z. Cao, K. Liu, X. Yin, N. Wang, P. Chen, *Org. Lett.* **2022**, *24*, 5497−5502.

[17] Y. Zhang, J. Sun, G. Zhuang, M. Ouyang, Z. Yu, F. Cao, G. Pan, P. Tang, C. Zhang, Y. Ma, *J. Mater. Chem. C* **2014**, *2*, 195−200.

[18] W. Luo, Y. Zhang, Y. Gong, Q. Zhou, Y. Zhang, W. Yuan, *Chin. Chem. Lett.* **2018**, *29*, 1533−1536.

[19] T. Yu, D. Ou, Z. Yang, Q. Huang, Z. Mao, J. Chen, Y. Zhang, S. Liu, J. Xu, M. R. Bryce, Z. Chi, *Chem. Sci.* **2017**, *8*, 1163−1168.

[20] W. Zhao, Z. Liu, J. Yu, X. Lu, J. W. Y. Lam, J. Sun, Z. He, H. Ma, B. Z. Tang, *Adv. Mater.* **2021**, *33*, 2006844−2006851.

[21] K. Chung, M. S. Kwon, B. M. Leung, A. G. Wong-Foy, M. S. Kim, J. Kim, S. Takayama, J. Gierschner, A. J. Matzger, J. Kim, *ACS Cent. Sci.* **2015**, *1*, 94−102.

[22] X. Zheng, Y. Zheng, L. Peng, Y. Xiang, A. Tong, *J. Phys. Chem. C* **2017**, *121*, 21610−21615.

[23] J. Yang, Z. Fu, H. Ma, T. Wang, Q. Li, K. Wang, L. Wu, P. Chen, H. Feng, B. Z. Tang, *ACS Mater. Lett.* **2023**, *5*, 1441−1449.

[24] T. Sachdeva, M. D. Milton, *Dyes Pigments* **2020**, *181*, 108539−108548.

[25] Y. Zheng, L. Zuo, L. Zhang, Z. Huang, S. Li, Z. Yang, Z. Mao, S. Luo, C. Liu, F. Sun, G. Shi, Z. Chi, B. Xu, *Chin. Chem. Lett.* **2022**, *33*, 4536−4540.

[26] Y. Zhang, J. Sun, X. Lv, M. Ouyang, F. Cao, G. Pan, L. Pan, G. Fan, W. Yu, C. He, S. Zheng, F. Zhang, W. Wang, C. Zhang, *CrystEngComm* **2013**, *15*, 8998−9002.

[27] K. Guo, F. Zhang, S. Guo, K. Li, X. Lu, J. Li, H. Wang, J. Cheng, Q. Zhao, *Chem. Commun.* **2017**, *53*, 1309−1312.

[28] Y.-X. Peng, Y.-T. Gan, R.-G. Shi, W. Huang, T. Tao, *J. Phys. Chem. C* **2018**, *122*, 29488−29497.

[29] Y. Gong, P. Zhang, Y. Gu, J. Wang, M. Han, C. Chen, X. Zhan, Z. Xie, B. Zou, Q. Peng, Z. Chi, Z. Li, *Adv. Optical Mater.* **2018**, *6*, 1800198−1800207.

[30] Y. Gong, S. He, Y. Li, Z. Li, Q. Liao, Y. Gu, J. Wang, B. Zou, Q. Li, Z. Li, *Adv. Optical Mater.* **2020**, *8*, 1902036−1902045.

[31] M.-Y. Zhang, Q. Peng, C.-H. Zhao, *J. Mater. Chem. C* **2021**, *9*, 1740−1745.

[32] G. Yang, W.-X. Zhao, J.-Y. Cao, Z.-M. Xue, H.-T. Lin, S.-H. Chen, T. Yamato, C. Redshaw, C.-Z. Wang, *Chem. Commun.* **2024**, *60*, 3966−3969.